Design of 2D Skyrmionic Metamaterial Through Controlled Assembly

Qichen Xu*,^{1,2} Zhuanglin Shen†,³ Alexander Edström†,^{1,2} I. P. Miranda†,⁴ Zhiwei Lu,¹ Anders Bergman,⁴ Danny Thonig,^{5,4} Wanjian Yin,⁶ Olle Eriksson,^{4,7} and Anna Delin^{1,2,8}

1 Department of Applied Physics, School of Engineering Sciences, KTH Royal
Institute of Technology, AlbaNova University Center, SE-10691 Stockholm, Sweden

2 Swedish e-Science Research Center, KTH Royal Institute of Technology, SE-10044 Stockholm, Sweden*

3 Key Laboratory of Quantitative Synthetic Biology, Shenzhen Institute of Synthetic Biology, Shenzhen
Institutes of Advanced Technology, Chinese Academy of Sciences, Shenzhen 518055, China[†]

4 Department of Physics and Astronomy, Uppsala University, Box 516, SE-75120 Uppsala, Sweden

5 School of Science and Technology, Örebro University, SE-701 82, Örebro, Sweden

6 College of Energy, Soochow Institute for Energy and Materials InnovationS (SIEMIS), and Jiangsu Provincial Key
Laboratory for Advanced Carbon Materials and Wearable Energy Technologies, Soochow University, Suzhou, 215006, China

7 Wallenberg Initiative Materials Science for Sustainability (WISE), Uppsala University, Box 516, SE-75120 Uppsala, Sweden

8 Wallenberg Initiative Materials Science for Sustainability (WISE),
KTH Royal Institute of Technology, SE-10044 Stockholm, Sweden

(Dated: February 19, 2024)

Despite extensive research on magnetic skyrmions and antiskyrmions, a significant challenge remains in crafting nontrivial high-order skyrmionic textures with varying, or even tailor-made, topologies. We address this challenge, by focusing on a construction pathway of skyrmionics metamaterial within a monolayer thin film and suggest several promising lattice-like, flakes-like, and cell-like skyrmionic metamaterials that are surprisingly stable. Central to our approach is the concept of 'simulated controlled assembly', in short, a protocol inspired by 'click chemistry' that allows for positioning topological magnetic structures where one likes, and then allowing for energy minimization to elucidate the stability. Utilizing high-throughput atomistic-spin-dynamic (ASD) simulations alongside state-of-the-art AI-driven tools, we have isolated skyrmions (topological charge Q=1), antiskyrmions (Q = -1), and skyrmionium (Q = 0). These entities serve as foundational 'skyrmionic building blocks' to forming reported intricate textures. In this work, two key contributions are introduced to the field of skyrmionic systems. First, we present a novel method for integrating control assembly protocols for the stabilization and investigation of topological magnets, which marks a significant advancement in the ability to explore new skyrmionic textures. Second, we report on the discovery of skyrmionic metamaterials, which shows a plethora of complex topologies that are possible to investigate theoretically and experimentally.

I. MAIN

Skyrmionic textures represent swirling topological spin configurations, typically stabilized by the Dzyaloshinskii–Moriya interaction (DMI). There are three primary skyrmionic textures: skyrmions[1–6], antiskyrmions[7–12], and skyrmioniums[13–15], distinguished by their topological charges, morphology and properties (such as the presence or not of skyrmion Hall effect). Moreover, recent studies have identified complex, higherorder skyrmionic textures carrying an absolute topological charge greater than 1[16–18]. The emergent physical properties of skyrmionic textures has great potential in design next generation sustainable spintronic applications such as neuromorphic computing[19], race-track memory[20], data encoding, and storage[21].

Advances in understanding interactions among skyrmionic textures, such as attraction, repulsion, and annihilation, resonate with the well-established principles of 'Click chemistry' [22]. 'Click chemistry' is

a process characterized by the synthesis of substances through the union of smaller units like molecules, with a focus on controlled assembly [23–33]. Expanding concept this to 'click magnetism', we introduce 'skyrmionic controlled assembly', utilizing skyrmions, antiskyrmions, and skyrmioniums as elemental skyrmionic building blocks. This methodology not only facilitates the integration of textures but also enables the creation of metastable magnetic textures from these building blocks.

These textures are similar to a class of artificial materials, namely metamaterials[34–36], which are defined by their custom-engineered configurations and bespoke building blocks, e.g., nanoscale wrinkles and split-ring Metamaterials are extensively applied in resonators. nanostructure designs across optics and plasmonics to develop sustainable applications and offer capabilities beyond those of conventional materials like negative refractive index. In this work, similar to the definition of metamaterials, we propose a skyrmionic metamaterial concept designed to accelerate the discovery of novel promising magnetic textures with intricate topologies for spintronics applications. We elaborate on this concept by detailing the creation of i) lattice-like skyrmionic metamaterial, which is a spin-texture lattice that possess a topo-

^{*} qichenx@kth.se

^{† †} These three authors contributed equally

logical charge greater than 1 within their primitive unit cells, as well as ii/flake-like skyrmionic metamaterial, large-scale high-order antiskyrmions with an underlying lattice structure, and iii/ cell-like skyrmionic metamaterial that incorporate a nesting of various texture types. Each of these promising magnetic textures showcases a non-trivial topology and is constructed from fundamental skyrmionic units. Based on the aforementioned 'Click chemistry' applied to skyrmionic textures, the key concept of our systematic exploration of skyrmionic metamaterials is also the controlled assembly, which enables the artificial placement of these elemental skyrmionic building blocks.

Employing spin-dynamics simulation tools in our controlled assembly protocols, we investigate the relative stability of the created skyrmionic metamaterials. Specifically, we perform high-throughput atomistic-spin-dynamic (ASD) simulations, using the UppASD package[37]. The material class we propose consists of a monolayer film, which inherently supports nontrivial topologies[16, 38–42]. We present a theoretical pathway for constructing various complex topological textures from skyrmionic building-blocks, including reported high-order antiskyrmions and skyrmion bags, as well as aforementioned skyrmionic metamaterial.

A. Local assembly and interaction profiles

For the design of controlled assembly simulations in a 2D skyrmionic system, it is imperative to first analyze pair-wise assembly, the stability of individual topological objects, and the interactions between the skyrmionic building blocks (e.g., skyrmions, antiskyrmions, and skyrmioniums). An efficient approach to study these behaviors involves examining the equilibrium and critical distances between skyrmionic building blocks and the distance dependence on the repulsion or attraction among them. In this study, we focus on metastable textures in a well known experimental system: Pd/Fe/Ir(111)[43–48]. A detailed discussion of the generalization of results can be found in Section IE. Unless it's said differently, the damping parameter in the ASD is 0.1 and we do all the simulations in a 3.5 T magnetic field. In this field, the basic state is ferromagnetic. We define the equilibrium distance as the minimal distance between two topological textures. Beyond this distance, the repulsive forces are insufficient to overcome the friction that may lead by damping or pinning force[49]. On the other hand, the critical distance represents a saddle point in the potential energy surface during the transition, marking the change from a state of non-interaction or extremely weak interaction to attraction.

To minimize thermal effects, which could introduce stochastic elements not central to this study, we set the simulation temperature at 1 mK. However, finite temperature effects are discussed in Appendix A2 to A8, along with supporting movies. Generally, with fixed interac-

tion parameters, a stronger applied field reduces both equilibrium and critical distances for combinations of skyrmions, antiskyrmions, and skyrmioniums, as shown in Figure 1 (a).

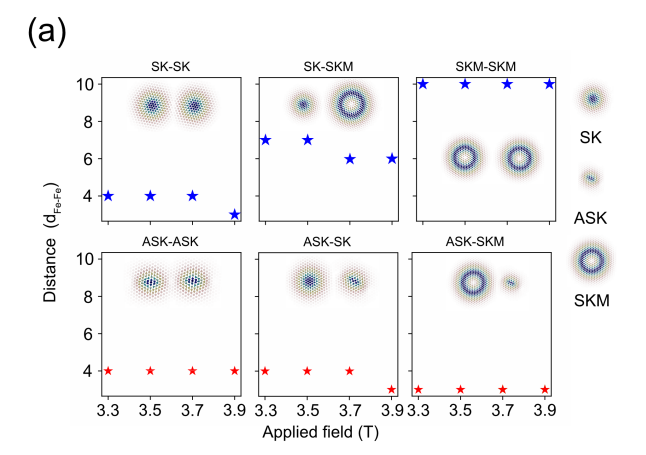
Delving deeper into the equilibrium distances, shown in the top three subfigures of Figure 1(a), we observe distinct behaviors. The combination of skyrmion and skyrmionium (middle figure, top panel of Fig.1a) exhibits isotropic outer boundaries, resulting in rotation-invariant repulsion. However, the dynamics between the different systems presented in Fig.1 differ. For instance, in skyrmion-skyrmion pairs, they separate until achieving an equilibrium distance through gyroscopic rotational dynamics[49].

In contrast, with skyrmion-skyrmionium pairs, only the skyrmionium moves while the skyrmion remains stationary. This immobility may be due to the skyrmion's strong friction, attributed to its directional topology [49].

When an antiskyrmion, characterized by anisotropic boundary, is part of the skyrmionic pair, the interaction behavior paradigm changes. Upon approaching the critical distance, non-interacting or weakly interacting components exhibit attraction, leading to assembly [50]. As depicted in the bottom three subfigures of Figure 1(a), two skyrmionic textures assemble when their initial gap is smaller than the critical distance, resulting in either a high-order antiskyrmion or a vanishing ferromagnetic state. During the assembly of two antiskyrmions, as illustrated in Figure 1(b), a metastable blocking point emerges. The concept of a blocking point is illustrated in Fig.8 (a). This object is in essence a quasi-equilibirum state that appears when two anti-skyrmionic textures are close enough and the self-rotation is prevented. Once a large enough lattice-like skyrmionic metamaterial is constructed, self-rotation becomes very difficult, since this would require the entire metamaterial to rotate. The result is that the lattice-like skyrmionic metamaterial becomes a very long-lived metastable state, despite its high complexity.

The blocking point, resembling a vortex-like connector with an inhomogeneous boundary and no integer topological charge, delays the assembly of antiskyrmion pairs by preventing self-rotation, creating a 'platform stage' in their temporal evolution (More information about the blocking point can be found in Appendix A2). This blocking point does not hinder assembly progression and is eventually overcome by the rotation of the antiskyrmions. The middle-bottom subplot of Figure 1(a) reveals that the assembly of skyrmion-antiskyrmion pairs results in a magnetic bubble without topological protection. This bubble formation is also depicted as a 'platform stage' in Figure 1(b).

The right-bottom subplot shows that the antiskyrmion-skyrmionium pair assembles when closer than their equilibrium distance, but the absence of a blocking point shortens the 'platform stage.' It should be noted that if the applied field is excessively strong,



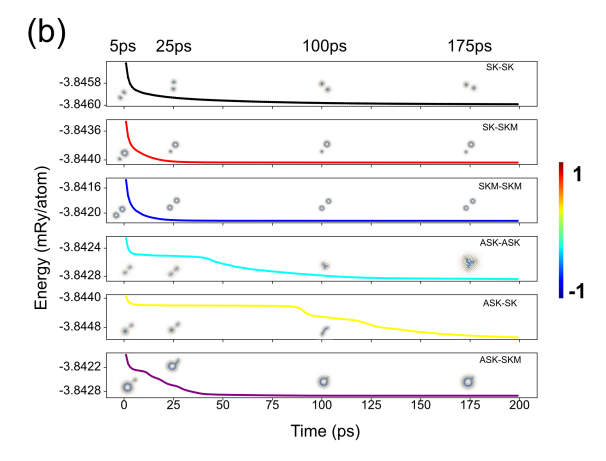


FIG. 1. (a) Pictorial representations of pair interaction dynamics as a function of applied magnetic field, for all pair-combinations of skyrmions, antiskyrmions, and skyrmionia. For comprehensive visualizations, we refer to the supplementary movies S1-S4. The red and blue stars indicate the calculated equilibrium distances for each pair as influenced by the external magnetic field, with distances expressed in units of the Fe-Fe equilibrium distance $d_{\text{Fe-Fe}} = 0.272 \,\text{nm}$. We have used blue stars to indicate that at the equilibrium distance, the pair interaction energy has a local minimum. Red stars, conversely, denote a critical distance (a saddle point in the PES), implying that for distances smaller than this critical distance, the spin textures either merge or annihilate. (b) This part of the figure illustrates the temporal evolution of the total energy for each pair assembly process, as derived from Atomistic Spin Dynamics (ASD) simulations. The y-axis quantifies the total energy. Accompanying subplots provide snapshots of the spin configurations during the assembly process. The adjoining colorbar clarifies the spin orientation in these configurations: a dark blue color (-1) signifies spins pointing downwards, away from the viewer, while a red color (1) represents spins pointing upwards, towards the viewer.

in the antiskyrmion-skyrmionium pair, the intense spin waves generated during assembly may destroy the skyrmionium, leaving only a single antiskyrmion. This increased likelihood of strong spin waves impacting the skyrmionium's boundary is attributed to the use of periodic boundary conditions in this study, simulating the effects of non-isolated cases and approximating experimental assembly processes more closely.

B. High-order antiskyrmion lattice

Three examples of surprisingly stable lattice-like skyrmionic metamaterials that we have discovered are shown in the top subfigures of Figure 2(b),(c), and (d). By using numerically prefabricated building blocks (see text below), i.e., high-order antiskyrmions with Q=-2, -5, and -12, it is possible to construct skyrmionic metamaterials, essentially similar to e.g. artificial spin-ice structures and lattice based metamaterials. Note that here high-order antiskyrmions represent magnetic textures with a topological charge Q < -1 [16, 51]. To quantify the stability of the skyrmionic metamaterials of Fig.2, we computed stability maps with temperature and external field as critical parameters. These stability maps are depicted at the bottom of Fig.2. Note that in these figures stability is marked as a blue region (also marked with a 1) while the white region, marked with a 0, denotes an unstable configuration, that dissolves with time. In this stability analysis we terminated the simulations

after 200 ps simulation time, and simply inspected if a configuration was stable by monitoring that it reached a static configuration. From this analysis we can draw a conclusion that the magnetic configurations are at least metastable. Interestingly, the stability analysis of Fig.2 show that lattices of higher order skyrmions can be stable over significant temperature and field ranges.

Below, we detail our approach for constructing and discovering long-lived lattice-like skyrmionic metamaterials. In essence, the first step is to construct high-order antiskyrmions (we will call them prefabricated building blocks from here on) from simple antiskyrmions. Then, these prefabricated building blocks are combined together in such a way that self-rotation is prevented, which in turn stabilized the resulting lattice-like skyrmionic metamaterial.

In this way we start by using single antiskyrmions to construct prefabricated building blocks via simulated controlled assembly. This prefabrication process is guided by the site-based topological charge distribution rule discussed in Section IG and the fact that antiskyrmions show an attractive interaction with other structures (skyrmion, skyrmionium, antiskyrmion), as demonstrated in Section IA. A subtle issue in the prefabrication process is how to place the antiskyrmions so that they assemble to the building block we want to fabricate. In the simulation, this is done by placing them at the appropriate distances from each other.

In an experimental setting, this may be realized using, for example, gradient magnetic fields [4, 52–55] or even

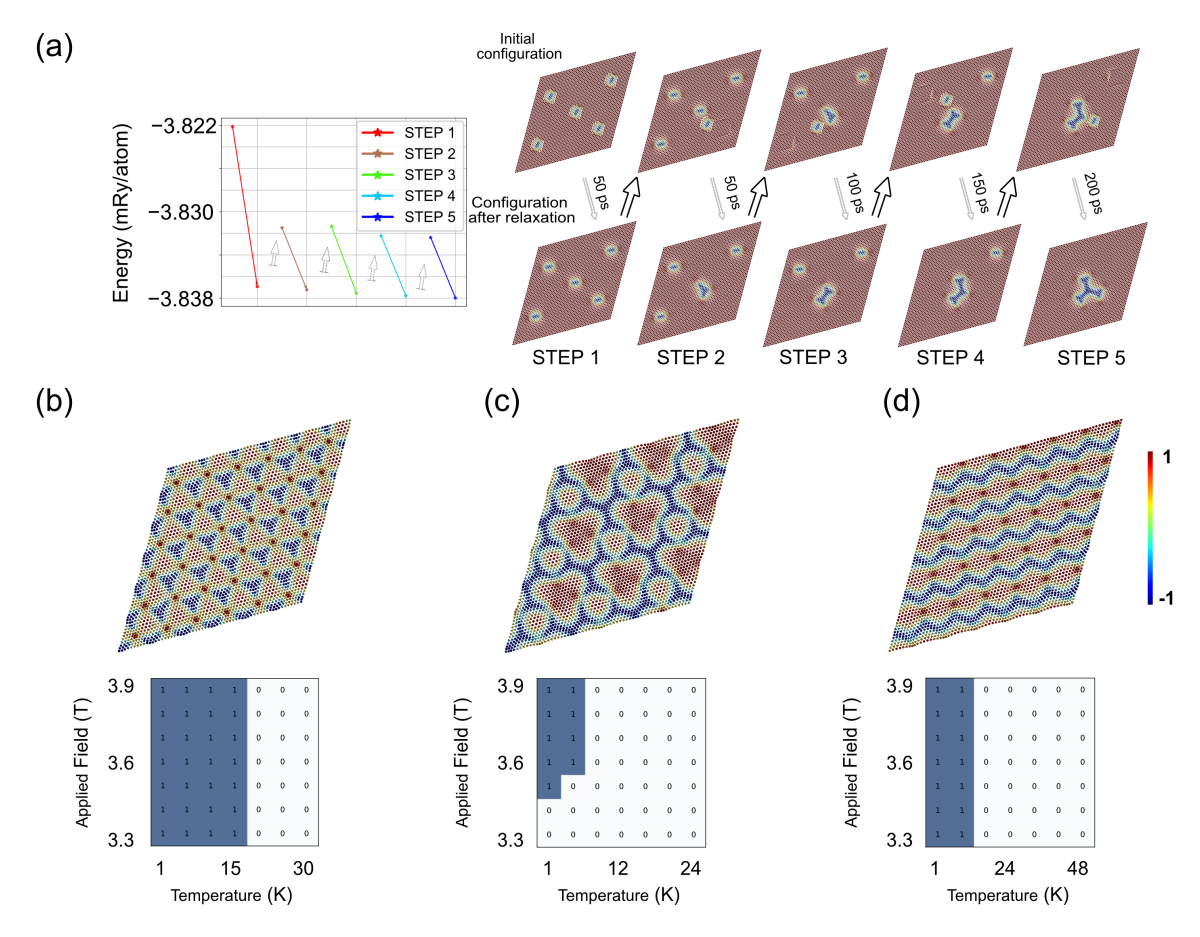


FIG. 2. Construction of high-order antiskyrmion (the prefabricated building block) and lattices from individual antiskyrmions. The ASD simulation system size is 60×60 spins. (a) Illustration of the step-by-step formation of a triangular high-order antiskyrmion via controlled assembly. The left diagram presents the initial- and post-relaxation energies at each stage, with relaxation times increasing from 50 ps (step 1) to 200 ps (step 5). Top and bottom subfigures display the corresponding initial and postrelaxation spin configurations. Blue indicates spins pointing downward, red signifies spins pointing upward, and white represents spins oriented along the plane. (b-d) Three distinct examples of array-like skyrmionic metamaterial, each stabilized via lattice embedding: (b) Top subfigure showcases the initial lattice embedding in real-space for an array-like skyrmionic metamaterial with Q = -2 high-order antiskyrmions, followed by a stability maps analysis in the bottom subfigure. A value of 1 indicates stability after 200 ps ASD simulation, while 0 denotes lattice disintegration. (c) An array-like skyrmionic metamaterial formed from Q = -5 high-order antiskyrmions. (d) An array-like skyrmionic metamaterial composed of Q = -12 high-order antiskyrmions. Additional details, along with supportive movies S5, S10, S11, and S13, can be found in Appendix A2.

temperature gradients [56]. In Figure 2(a) we give one example on how to fabricate a Q = -5 high-order antiskyrmion, with five controlled-assembly steps, starting from five isolated antiskyrmions. Thus, the triangle-like high-order antiskyrmion (Q = -5) is fabricated by controlled placement of antiskyrmions, followed by consecutive relaxations of the spin structure using ASD. How the energy changes with each step is illustrated in the left part of Figure 2(a). This result indicates a feasible dynamic construction method for building high-order antiskyrmions: sequentially manipulating pre-generated antiskyrmions. Once we have constructed the prefabricated building blocks, these can be used to construct lattice-like skyrmionic metamaterials. Numerouse structures are of course possible, and which lattice-like skyrmionic metamaterial will result depends on the relative placement of the prefabricated building blocks. For instance, in order to create a lattice-like skyrmionic metamaterial with a hexagonal lattice as shown in Figure 2(b), the prefabricated building blocks are placed so that they form a hexagonal lattice.

C. Flake-like skyrmionic metamaterials

Together with the aforementioned lattice-like skyrmions metamaterial, another possible stable type that suggested in this work is the *flakes* which is shown in the middle subfigure of Figure 3(c) and (d). To demonstrate the building pathway of a flake, we begin by constructing ring-like prefabricated building blocks (Q = -6). As shown on the left of Figure

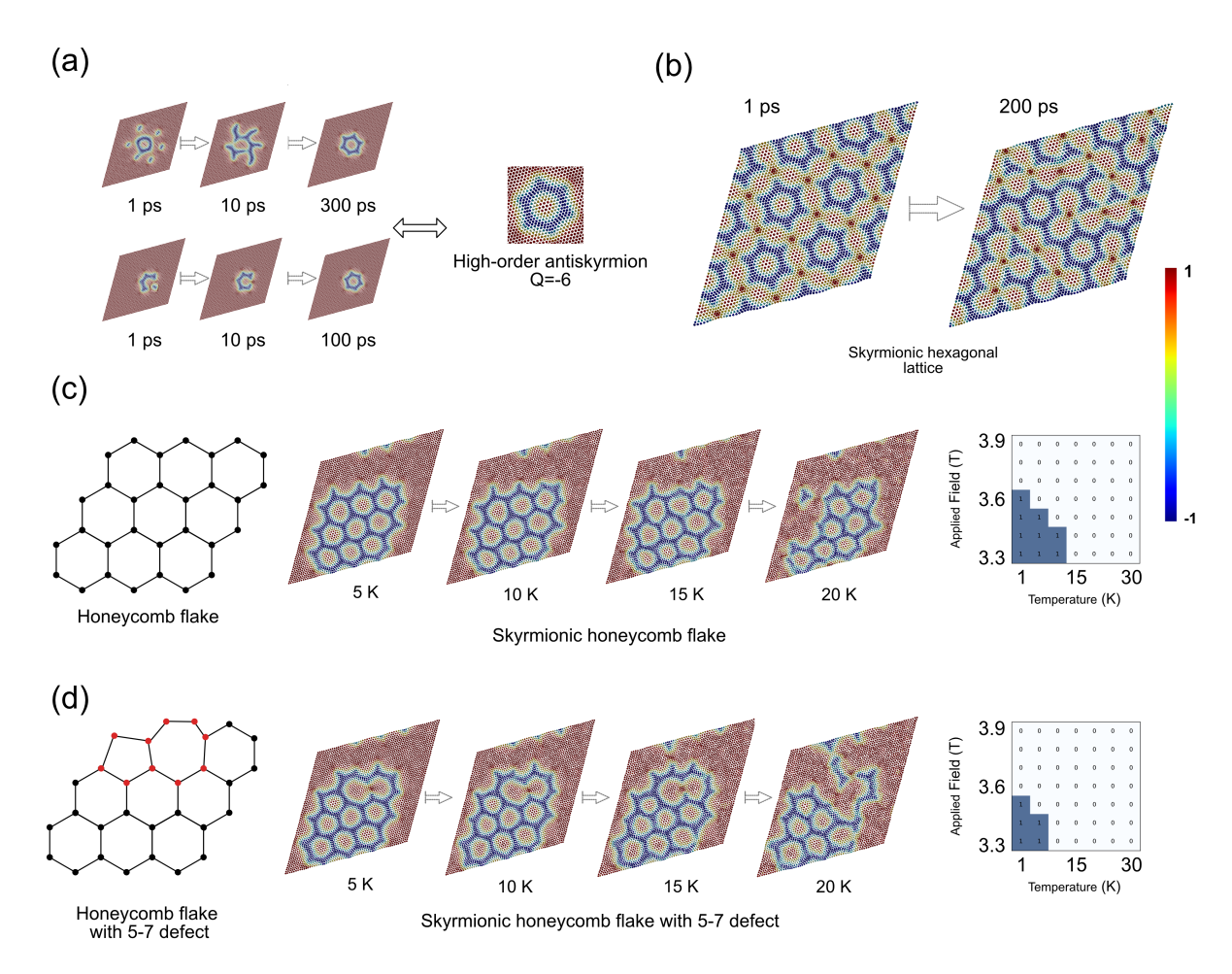


FIG. 3. (a) Two distinct methodologies for assembling a high-order ring-shaped antiskyrmion with Q=-6. The top pathway involves combining six antiskyrmions with one skyrmionium, whereas the bottom pathway utilizes one high-order antiskyrmion (Q=-5) paired with an additional antiskyrmion. (b) Temporal progression of a skyrmionic honeycomb lattice at 1 K. The left image depicts the initial spin configuration, while the right image illustrates the state after 200 ps ASD time evolution. (c) and (d) The left-most panel presents a flawless honeycomb flake-like skyrmionic metamaterial alongside a variant with 5-7 ring defects (indicated by red dots). The central subplots in (c) and (d) display the real-space spin configurations of a skyrmionic honeycomb flake after 200 ps ASD simulations at four distinct temperatures. The far-right panels in (c) and (d) showcase the respective stability phase diagrams. Here, a value of 1 indicates stability after 200 ps ASD simulations, while 0 denotes that the flake vanished. In all shown spin configuration maps, blue denotes spins pointing downward (away from the viewer), red signifies spins pointing upward (towards the viewer), and white represents spins aligned along the plane.

3(a), according to the site-based topological charge distribution rule, there are two methods for forming this 'ring' structure. In the first method (top of Figure 3(a)), six antiskyrmions (Q=-1) are positioned close enough, less than the critical distance, to the boundary of a skyrmionium (Q=0) to ensure simultaneous attraction. A 300 ps spin dynamics simulation on this initial spin configuration predicts the assembly of the antiskyrmions, forming the target prefabricated building block with a total topological charge of -6. The second method (bottom of Figure 3(a)) involves moving an antiskyrmion close to the notch of a crescent-shaped prefabricated building block (Q=-5), created from 5 antiskyrmions. In this case, only 100 ps ASD simulations are required to validate the formation of the target

high-order antiskyrmion flake.

After acquiring this high-order antiskyrmion, we use it as an elementary building block to construct a high-order antiskyrmion lattice, as shown in Figure 3(b). This skyrmionic lattice is predicted to be unstable even at 1 K, where a minor self-rotation can easily move the blocking point, leading to connections between components and unwinding. During this process, we also observe the formation of some flake-like textures.

Expanding on this, we increase the antiskyrmion density based on the previous building block. Ultimately, as shown in Figure 3(c), we isolate a honeycomb flake-like skyrmionic metamaterial (Q = -22). In Figure 3(d), by adding one more antiskyrmion, we obtain a honeycomb flake-like skyrmionic metamaterial (Q = -23) hosting

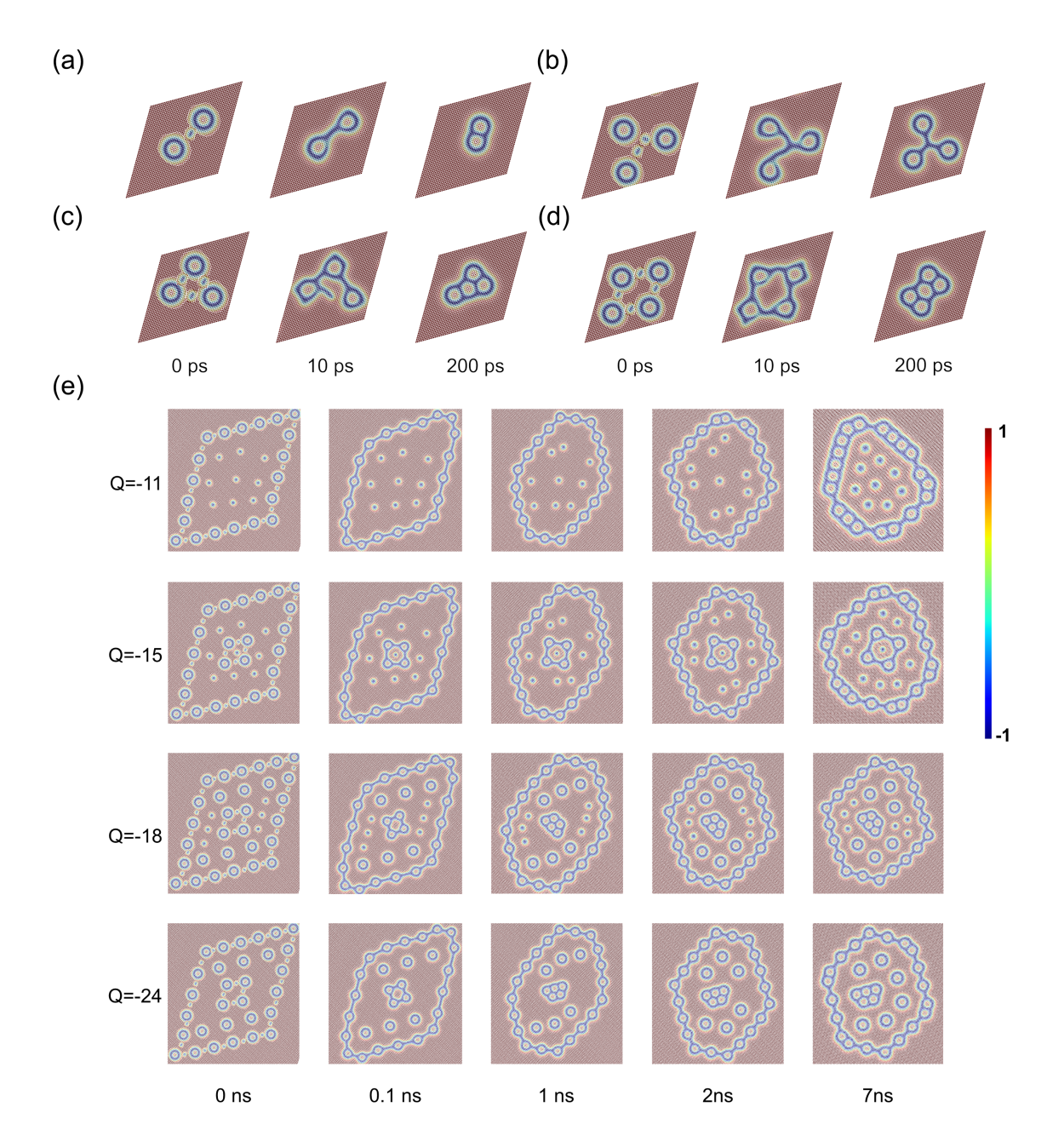


FIG. 4. (a-d) Snapshots from ASD simulations showing assembly behaviors with different initial conditions. These textures include skyrmion bags with topological charges ranging from -1 to -4. (e) Snapshots from ASD simulations showing assembly behaviors with different initial conditions. These textures include skyrmion bags with topological charges ranging from -11 to -24. The color scale applies to subplots (a), (g), (h), (i), and (j), where -1 indicates spins pointing downwards (away from the viewer) and 1 indicates spins pointing upwards (towards the viewer). Further details and supporting movies (S16-S19).

the well-known 5-7 honeycomb lattice defects[57], where a 5-7 defect in a honeycomb lattice, is a defect in which one ring has 5 sites and an adjacent ring has 7 sites, instead of all rings having 6 sites. Both of those flake-like skyrmionic metamaterial are predicted to be stable even at 10K in Pd/Fe/Ir (111). However, the flake with the 5-7 defect is less stable than the one without. To further analyze this, we define the relative defect formation

energy as:

$$E_{rdf} = (E_{hf} + n \times (E_{ASK} - E_{FM}) - E_{df})/n \tag{1}$$

Here, E_{rdf} , E_{hf} , E_{FM} , E_{ASK} , and E_{df} represent the relative defect formation energy, the energy of the honeycomb flake-like skyrmionic metamaterial under a ferromagnetic background, the energy of the ferromagnetic background, the energy of an isolated antiskyrmion under a ferromagnetic background, and the energy of the honey-

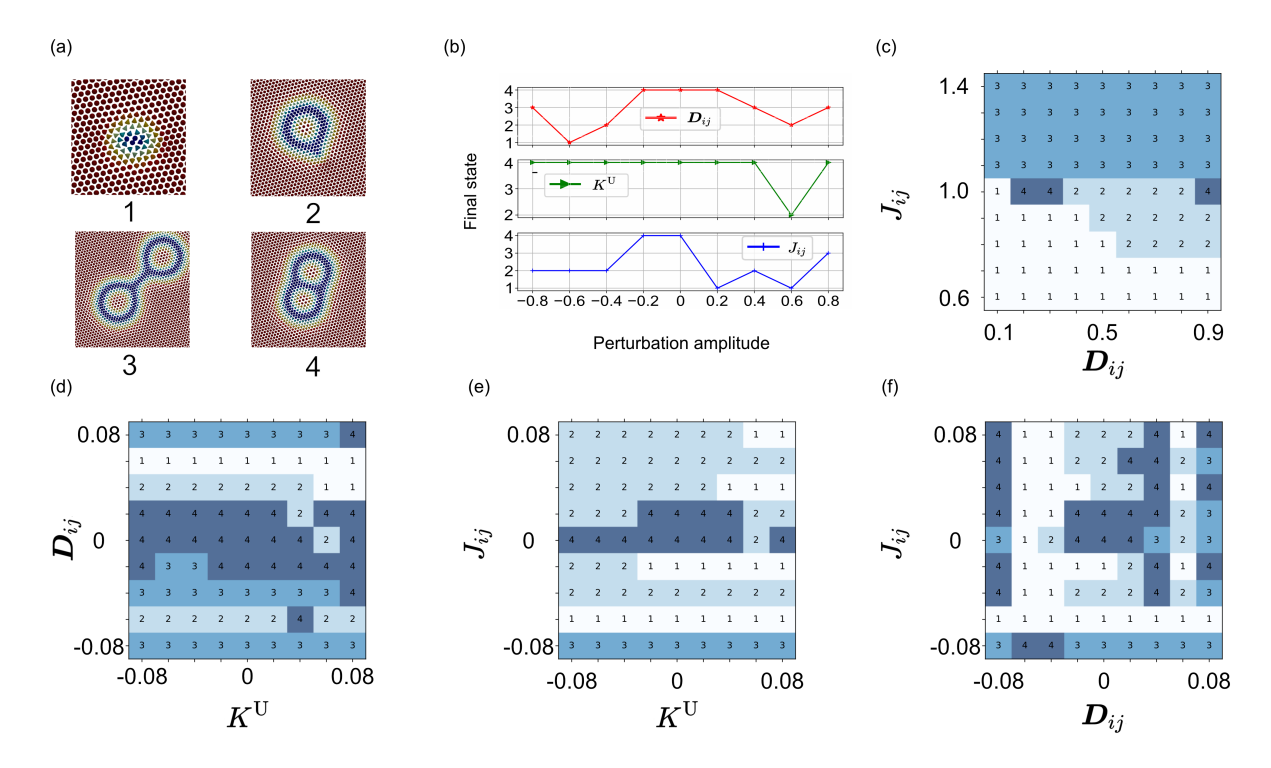


FIG. 5. Tests of the robustness and genericity of the controlled assembly process. (a) Subplots 1 to 4 display the final states after 200 ps. The initial state, consisting of two skyrmionium and one antiskyrmion, is the same for all four subplots.(b) Results under random perturbations of varying maximum amplitudes on each nearest shell applied to \mathbf{D}_{ij} , J_{ij} , and K^U . (c) Final states after scaling of the exchange interaction parameters J_{ij} and damping, following 200 ps ASD simulations. The color from white to dark blue and the inside number from 1 to 4 indicates the final state 1 to 4 that is displayed in (a). (d-f) Final states with random perturbations applied to combinations of \mathbf{D}_{ij} - K^U , J_{ij} - K^U , and J_{ij} - \mathbf{D}_{ij} , respectively.

comb flake-like skyrmionic metamaterial with a 5-7 defect under a ferromagnetic background, respectively. The n in the formula denotes the topological charge difference between the two flakes. The DFT calculated magnetic spin moment, m_s , was 2.78 $\mu_B/{\rm atom}$ of each Fe site. As a consequence the relative defect formation energy between the two flakes, when interaction with an applied field of 3.5 Tesla, is ~ 0.15 mRy/defect, indicating that introducing defects to the flake-like skyrmionic metamaterial decreases its stability.

D. Stablized cell-like skyrmionic metamaterial with texture nesting

To optimize the use of all basic building blocks relevant for this investigation, namely skyrmions, antiskyrmions, and skyrmionium, as shown in Figure 4(e) this section suggests several promising cell-like skyrmionic metamaterials and explores the construction pathway from small skyrmion bags to cell-like skyrmionic metamaterials, taking inspiration from the design of a skyrmion bag[58]. Since these bags can also be interpreted as magnetic textures stabilized by skyrmionium. As demonstrated in Figure 4(a) to (d), we have been able to stabilize several skyrmions with different complexity and topological

charges. This involves, e.g., skyrmion bags with topological charge ranging from -1 to -4, by applying a controlled assembly approach to sets of skyrmionium and antiskyrmions. Note that the information in Fig.4 shows the time evolution of the different topological objects, where at 0 ps show the configuration obtained initially in the controlled assembly protocol, and the data at 200 ps (Fig.4a-d) shows the final converged configuration. We observe that in the so conducted, controlled assembly process, the textures inherit a homogenous boundary from the skyrmionium, lose the property of attraction but retain their topological charge. Since these skyrmion bags also adhere to the local topological charge distribution, it is expected that more complex skyrmion bags can be constructed through similar operations.

With the introduction of these new kinds of prefabricated building blocks, i.e., skyrmion bags, the repertoire of building blocks with isotropic boundary conditions, or in other words, those that exhibit mutual repulsion, is now expanded beyond the initial three types. Utilizing these building blocks, we introduce a texture nesting operation, which involves using antiskyrmions and skyrmionium to create line-like, closely-packed skyrmion bags as boundaries to nest other textures with isotropic boundary conditions. As shown in Figure 4(e), we conduct a 7 ns ASD simulation in a system of 300×300 spins. Due to

the large system size and extended simulation time, we set the damping to 0.2 and the time step to 1 fs to expedite convergence. We design a texture, similar to but not identical to one in a previous study[17], containing only skyrmions within the skyrmion-bag-ring. This results in a skyrmion bag with a skyrmion lattice inside. Subsequently, we experiment with embedding skyrmionium and small skyrmion bags within the larger skyrmion bag ring, as illustrated in the subsequent rows of Figure 4(e). This controlled assembly mechanism potentially leads to more complex metastable textures on demand. All these dynamic pathways can be summarized as utilizing repulsion from skyrmions and skyrmion bags to inhibit the shrinking process of a newly assembled skyrmion bag.

E. Generalization of results

Until now, all simulations have been performed using spin Hamiltonian parameters for Pd/Fe/Ir(111) calculated from Density Functional Theory (DFT) [48]. These calculations are known to give rather precise values of the Heisenberg exchange as well as anisotropic exchange (e.g. Dzyaloshinskii-Moriya interaction (DMI)), but as with all theory, a smaller numerical uncertaintly is naturally possible. In order to test the sensitivity of the here predicted results towards such errors we designed a set of simulations where the parameters we scaled. This also generalizes the controlled assembly protocols to a broader material space. Hence, we designed a set of simulations involving two skyrmioniums and one antiskyrmion, applying scaling and perturbation operations to the DFT calculated parameters of Pd/Fe/Ir(111). Four final states (1-4) after 100 ps ASD simulation are shown in Figure 5(a) subplot 1 to 4.

In these simulations, as illustrated in Figure 5(b), we first applied randomly perturbation on DFT calculated DMI (\mathbf{D}_{ij}) , anisotropy (K^{U}) , or Heisenberg exchange (J_{ij}) with maximum amplitude from -0.8 to 0.8, respectively. In all simulations of this section, we used a system of 60×60 spins in a 3.5 Tesla magnetic field. For these simulation parameters, we performed 100 ps ASD simulations at each sampling point. We could find the final state 4 is not strictly limited to the originally DFT calculated parameters.

Furthermore, to evaluate the generalization under pairwise change of two different kind of spin coupling, e.g., \mathbf{D}_{ij} - J_{ij} pair. as shown in Figure 5(c) we first scaled the DFT calculated nearest-neighbor J_{ij} from 0.6 to 1.4 and varied the preset damping (originally 0.1) from 0.1 to 0.9. The results indicate that with lower J_{ij} and higher damping, we can successfully form a skyrmion bag. However, increasing J_{ij} leads to more energetic spin wave emissions from the assembly process, which can destabilize structures like skyrmioniums and skyrmion bags compared to antiskyrmions. Interestingly, when J_{ij} is lower, 100 ps may not suffice for the skyrmion bag to transition from a sparse state (as shown in subplot 3 in Figure 5(a)) to a

dense state (as shown in subplot 4 in Figure 5(a)). From a damping perspective, lower damping results in longer spin wave lifetimes, thereby increasing the likelihood of metastable textures vanishing due to interactions with spin waves. With this insight, we reverted the Gilbert damping to its original setting ($\alpha = 0.1$) to mitigate the effects of spin waves. We then analyzed the dynamics of controlled assembly with perturbed interaction parameters, such as \mathbf{D}_{ij} , J_{ij} , and K^{U} .

Similar generalization tests are performed in \mathbf{D}_{ij} - K^{U} , J_{ij} - K^{U} , and \mathbf{D}_{ij} - J_{ij} pairs, as shown from Figure 5(d) to Figure 5(f), it becomes evident that the results are not limited to the DFT calculated parameters of the Pd/Fe/Ir(111) system. Skyrmion metamaterial and controlled assembly are anticipated to occur in other systems where long-range frustration and DMI interactions coexist.

F. Discussion and Conclusion

The ability to use simulation tools to pick up individual atoms and to place them where one wants, so that one can then investigate their possible interaction and stability, has been a fantastic asset in understanding chemical reactions, and therefore deepened the understanding of e.g. catalysis, crystal growth and surface reconstructions. Several softwares have been designed for this task. The ability to do this with magnetic textures is far less investigated. Here we take steps to accommodate this, and we demonstrate that controlled assembly protocols, that combine artificial intelligence based segmentation tools with atomistic spin-dynamics simulations, offer a great opportunity for such investigations. In this work we began by systematically analyzing the pairwise interactions between skyrmionic elements, pinpointing their critical distances. This understanding facilitate the exploration of single high-order antiskyrmion formation through controlled assembly, guided by the distribution of site-based local topological charges. Crucially, we also employed the concept of lattice embedding, and successfully identified and characterized a variety of skyrmionic metamaterials. These structures are notable for their stability for a wide range of different Heisenberg and DM interactions, presenting new realms of complexity and stability in magnetic textures. The interactions used for the majority of the investigations presented here, represent a system that has been realized in experimental works; the Pd/Fe/Ir(111) system. Hence, the spin Hamiltonian used here is appropriate for a system that has been observed in nature, as opposed to a model Hamiltonian where the interaction parameters may be tuned or fitted, having a specific finding or observation in mind. Judging from the results presented here, the Pd/Fe/Ir(111) system has a fantastic richness in it, in terms of the topological magnetic structures it can host.

The findings presented here not only contribute to the theoretical landscape of skyrmionics but also open

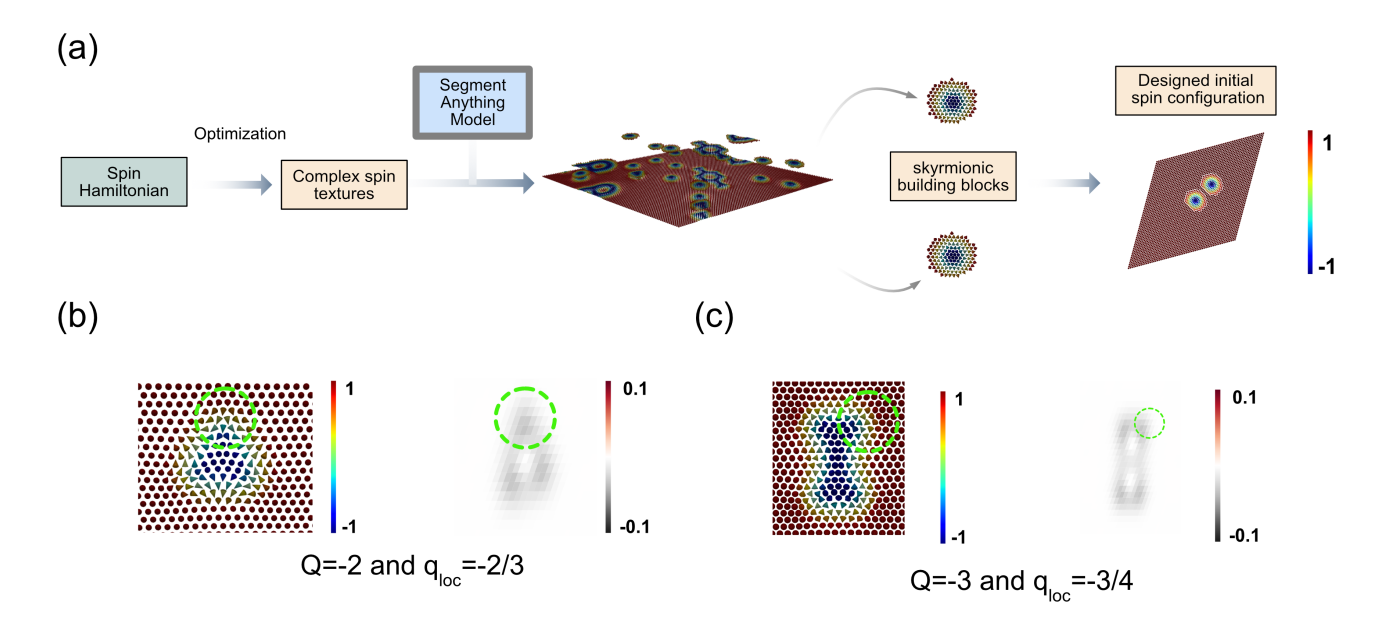


FIG. 6. (a) Workflow for constructing initial spin configurations for controlled assembly analysis. (b) and (c) Visualization of site-based local topological charge distribution ($q_{\rm loc}$, see Methods). The left panel features real-space visualizations of the magnetic texture, while the right panel depicts the correspondent topological charge density. The color bars ranges are given in terms of the z-component for the local normalized spin moment (left panel), and the site-based topological charge density (right panel, unitless). Green dashed circles mark the sites, highlighting the local environment. For the Q=-2 structure, the cutoff radius of $r_c \sim 0.9$ nm results in $q_{\rm loc} \sim -\frac{2}{3}$.

promising avenues for the practical realization of long-lived complex magnetic textures. Constructing these textures from fundamental skyrmionic configurations paves the way for innovative applications in spintronics. We hope that our work will catalyze experimental explorations, further advancing the development of future spintronic devices.

G. Methods

We describe this system using a classical atomistic spin Hamiltonian, with all relevant parameters derived from Density Functional Theory (DFT)[16, 48]:

$$\mathcal{H} = -\sum_{i \neq j} J_{ij} \mathbf{S}_i \cdot \mathbf{S}_j - \sum_{i \neq j} \mathbf{D}_{ij} \cdot (\mathbf{S}_i \times \mathbf{S}_j)$$
$$-\sum_{i} \mu_i \mathbf{B}^{\text{ext}} \cdot \mathbf{S}_i - \sum_{i} K_i^{\text{U}} (\mathbf{S}_i \cdot \mathbf{e}_z)^2,$$
(2)

where \mathbf{S}_i represents the normalized spin moment at site i, and μ_i its magnetic moment length. The parameters J_{ij} , \mathbf{D}_{ij} , K^{U} , \mathbf{e}_z , and $\mathbf{B}^{\mathrm{ext}}$ correspond to Heisenberg exchange interactions, Dzyaloshinskii–Moriya interactions, uniaxial anisotropy, the easy axis vector, and the applied field, respectively. The DFT calculated parameters are scaled and perturbed in the generalization section using preset factors and restricted Gaussian noise. This is done to enhance the model's generalizability and robustness.

The stability test, involving perturbation of input parameters, demonstrates that our findings are not limited to the Pd/Fe/Ir system but also applicable to a broader range of skyrmion-hosting thin-film materials.

Using this spin Hamiltonian, we performed highthroughput atomistic spin dynamics (ASD) simulations across a wide array of initial spin configurations. These configurations, where skyrmionic particles are separated by various distances, help us understand their interaction behavior paradigm. To facilitate this, as shown in Figure 6(a), we employed a state-of-the-art artificial intelligence segmentation tool to extract elemental spin textures from the optimized larger spin system[16, 59]. This tool allows for the systematic design of initial spin textures. such as selecting different element textures, altering distances between elements, and rotating element textures. We studied the motion of skyrmionic textures at T = 1mK using atomistic spin dynamics, numerically solving the stochastic Landau–Lifshitz–Gilbert (LLG) equation implemented in the UppASD package[37]:

$$\frac{d\mathbf{S}_{i}}{dt} = -\gamma_{L}\mathbf{S}_{i} \times \left(\mathbf{B}_{i} + \mathbf{B}_{i}^{f}\right) - \gamma_{L}\frac{\alpha}{S_{i}}\mathbf{S}_{i} \times \left[\mathbf{S}_{i} \times \left(\mathbf{B}_{i} + \mathbf{B}_{i}^{f}\right)\right]$$
(3)

Here, S_i represent the norm of \mathbf{S}_i and \mathbf{B}_i is the effective magnetic field:

$$\mathbf{B}_{i} = -\frac{\partial \mathcal{H}}{\partial \mathbf{S}_{i}} \tag{4}$$

Here $\mathbf{B}_i^{\mathrm{f}}$ denotes the stochastic magnetic field. γ is the gyromagnetic ratio, and we use the renormalized gyromagnetic ratio $\gamma_L = \frac{\gamma}{(1+\alpha^2)}$ in this work. The scalar Gilbert damping constant, α , is adjusted in our study.

As depicted in Figure 6(b) and (c), we propose a protocol to guide the construction of all skyrmionic metamaterials in 2D films, utilizing a site-based topological charge distribution method. In this context, a 'site' is a qualitative idea that refers to a representative piece of the texture, characterized by a unique local topological charge density distribution. A total of four distinct sites have been defined in this work, with more detailed information available in Appendix A3.

The topological charge Q of a given continuous twodimensional magnetization texture with unitary local direction $\vec{n}(x,y)$ is computed using

$$Q = \frac{1}{4\pi} \int_{A} \vec{n} \cdot \left(\frac{\partial \vec{n}}{\partial x} \times \frac{\partial \vec{n}}{\partial y} \right) dx dy, \tag{5}$$

where the integral is taken over the area A in the xyplane. Similarly, for a discrete spin system, one can use
the Berg and Lüscher invariant derivation [60], which
reads

$$Q = \sum_{x^*} q(x^*),\tag{6}$$

for all unique topological densities $q(x^*)$ attached to vertices x^* in the lattice with spins sitting around, also taking into account the periodic boundary conditions. By construction, both Eqs. 5 and 6 result in the total topological charge existent in the system. The discrete format allows to construct the concept of a local topological charge, q_{loc} , which can be defined as the following summation:

$$q_{\text{loc}} = \sum_{x^* \in \{x | r(x) \le r_c\}} q(x^*), \tag{7}$$

where r(x) denotes the distance of the point x from a reference point in the lattice, and r_c represents a cutoff radius. In this case, obviously $\lim_{r_c \to \infty} q_{\text{loc}} = Q$.

II. DATA AVAILABILITY

Data displayed in the plots are made available as a supplemental file. Further details and explanations of the data are available from the authors upon reasonable request.

III. CODE AVAILABILITY

The atomistic code used to apply spin dvnamic simulation can be https://github.com/UppASD/UppASD, and the code used for 2D spin texture segmentation can be found https://github.com/facebookresearch/segmentanything. The code for the visualization can be found at:https://github.com/MXJK851/SpinView/[61].

ACKNOWLEDGMENTS

Fruitful discussions with Filipp N. Rybakov (Uppsala University), Manuel Pereiro (Uppsala University) are acknowledged. We also thank Liuzhen Yang (Stockholm University) for the peer review teamwork. Financial support from the Swedish Research Council (grant numbers VR 2016-05980, VR 2019-05304, and 2023-04239), and the Knut and Alice Wallenberg foundation (grant numbers 2018.0060, 2021.0246, and 2022.0108) is acknowledged. A.D. and O.E. acknowledge support from the Wallenberg Initiative Materials Science for Sustainability (WISE), funded by the Knut and Alice Wallenberg Foundation (KAW). Q.X. acknowledges financial support from the China Scholarship Council (201906920083). The computations were enabled by resources provided by the National Academic Infrastructure for Supercomputing in Sweden (NAISS) and the Swedish National Infrastructure for Computing (SNIC) at NSC and PDC, partially funded by the Swedish Research Council through grant agreements no. 2022-06725 and no. 2018-05973. GPU resources are provided by KAW (Berzelius-2022-141).

(2019)

^[1] K. Huang, D.-F. Shao, and E. Y. Tsymbal, Nano Letters 22, 3349 (2022).

^[2] Y. Ba, S. Zhuang, Y. Zhang, Y. Wang, Y. Gao, H. Zhou, M. Chen, W. Sun, Q. Liu, G. Chai, et al., Nature Communications 12, 322 (2021).

^[3] N. Romming, C. Hanneken, M. Menzel, J. E. Bickel, B. Wolter, K. von Bergmann, A. Kubetzka, and R. Wiesendanger, Science 341, 636 (2013).

^[4] A. Casiraghi, H. Corte-León, M. Vafaee, F. Garcia-Sanchez, G. Durin, M. Pasquale, G. Jakob, M. Kläui, and O. Kazakova, Communications Physics 2, 145

^[5] K. Zeissler, S. Finizio, C. Barton, A. J. Huxtable, J. Massey, J. Raabe, A. V. Sadovnikov, S. A. Nikitov, R. Brearton, T. Hesjedal, et al., Nature communications 11, 428 (2020).

^[6] Y. Wang, T. Kitamura, J. Wang, H. Hirakata, and T. Shimada, Physical Review Applied 18, 014049 (2022).

^[7] M. Stier, W. Häusler, T. Posske, G. Gurski, and M. Thorwart, Physical Review Letters 118, 267203 (2017).

- [8] P. Siegl, M. Stier, A. F. Schäffer, E. Y. Vedmedenko, T. Posske, R. Wiesendanger, and M. Thorwart, Physical Review B 106, 014421 (2022).
- [9] F. Zheng, N. S. Kiselev, L. Yang, V. M. Kuchkin, F. N. Rybakov, S. Blügel, and R. E. Dunin-Borkowski, Nature Physics 18, 863 (2022).
- [10] K. Karube, L. Peng, J. Masell, X. Yu, F. Kagawa, Y. Tokura, and Y. Taguchi, Nature Materials 20, 335 (2021).
- [11] U. Ritzmann, S. von Malottki, J.-V. Kim, S. Heinze, J. Sinova, and B. Dupé, Nature Electronics 1, 451 (2018).
- [12] S. Huang, C. Zhou, G. Chen, H. Shen, A. K. Schmid, K. Liu, and Y. Wu, Physical Review B 96, 144412 (2017).
- [13] X. Zhang, J. Xia, Y. Zhou, D. Wang, X. Liu, W. Zhao, and M. Ezawa, Physical Review B 94, 094420 (2016).
- [14] S. Zhang, F. Kronast, G. van der Laan, and T. Hesjedal, Nano letters 18, 1057 (2018).
- [15] S. Li, J. Xia, X. Zhang, M. Ezawa, W. Kang, X. Liu, Y. Zhou, and W. Zhao, Applied Physics Letters 112, 142404 (2018).
- [16] Q. Xu, I. Miranda, M. Pereiro, F. N. Rybakov, D. Thonig, E. Sjöqvist, P. F. Bessarab, A. Bergman, O. Eriksson, P. Herman, et al., Physical Review Research 5, 043199 (2023).
- [17] D. Foster, C. Kind, P. J. Ackerman, J.-S. B. Tai, M. R. Dennis, and I. I. Smalyukh, Nature Physics 15, 655 (2019).
- [18] L. Desplat, J.-V. Kim, and R. L. Stamps, Physical Review B 99, 174409 (2019).
- [19] K. M. Song, J.-S. Jeong, B. Pan, X. Zhang, J. Xia, S. Cha, T.-E. Park, K. Kim, S. Finizio, J. Raabe, et al., Nature Electronics 3, 148 (2020).
- [20] A. Fert, N. Reyren, and V. Cros, Nature Reviews Materials 2, 1 (2017).
- [21] Y. Tokura and N. Kanazawa, Chemical Reviews 121, 2857 (2020).
- [22] H. C. Kolb, M. Finn, and K. B. Sharpless, Angewandte Chemie International Edition 40, 2004 (2001).
- [23] S. Lee, K. Sim, S. Y. Moon, J. Choi, Y. Jeon, J.-M. Nam, and S.-J. Park, Advanced Materials 33, 2007668 (2021).
- [24] F. Ishiwari, Y. Shoji, and T. Fukushima, Chemical Science 9, 2028 (2018).
- [25] J. E. ten Elshof, H. Yuan, and P. Gonzalez Rodriguez, Advanced energy materials 6, 1600355 (2016).
- [26] Z. Li, F. Yang, and Y. Yin, Advanced Functional Materials 30, 1903467 (2020).
- [27] P. Tierno, Physical chemistry chemical physics 16, 23515 (2014).
- [28] G. M. Whitesides and B. Grzybowski, Science 295, 2418 (2002).
- [29] M. Grzelczak, J. Vermant, E. M. Furst, and L. M. Liz-Marzán, ACS nano 4, 3591 (2010).
- [30] L. MacFarlane, C. Zhao, J. Cai, H. Qiu, and I. Manners, Chemical Science 12, 4661 (2021).
- [31] A. Levin, T. A. Hakala, L. Schnaider, G. J. Bernardes, E. Gazit, and T. P. Knowles, Nature Reviews Chemistry 4, 615 (2020).
- [32] N. J. Penfold, J. Yeow, C. Boyer, and S. P. Armes, ACS Macro Letters 8, 1029 (2019).
- [33] K. Das, L. Gabrielli, and L. J. Prins, Angewandte Chemie International Edition 60, 20120 (2021).
- [34] O. Hess, J. B. Pendry, S. A. Maier, R. F. Oulton, J. M. Hamm, and K. L. Tsakmakidis, Nature materials 11,

- 573 (2012).
- [35] N. I. Zheludev and Y. S. Kivshar, Nature materials 11, 917 (2012).
- [36] H. Zhao, B. A. Malomed, and I. I. Smalyukh, Nature Communications 14, 4581 (2023).
- [37] O. Eriksson, A. Bergman, L. Bergqvist, and J. Hellsvik, Atomistic spin dynamics: Foundations and applications (Oxford university press, 2017).
- [38] X. Zhang, J. Xia, Y. Zhou, X. Liu, H. Zhang, and M. Ezawa, Nature communications 8, 1717 (2017).
- [39] J. Tang, Y. Wu, W. Wang, L. Kong, B. Lv, W. Wei, J. Zang, M. Tian, and H. Du, Nature Nanotechnology 16, 1086 (2021).
- [40] C. Kind, S. Friedemann, and D. Read, Applied Physics Letters 116, 022413 (2020).
- [41] F. N. Rybakov and N. S. Kiselev, Physical Review B 99, 064437 (2019).
- [42] V. M. Kuchkin, B. Barton-Singer, F. N. Rybakov, S. Blügel, B. J. Schroers, and N. S. Kiselev, Physical Review B 102, 144422 (2020).
- [43] Q. Xu, Z. Shen, M. Pereiro, P. Herman, O. Eriksson, and A. Delin, arXiv preprint arXiv:2301.00207 (2022).
- [44] N. Romming, C. Hanneken, M. Menzel, J. E. Bickel, B. Wolter, K. von Bergmann, A. Kubetzka, and R. Wiesendanger, Science 341, 636 (2013).
- [45] D. M. Crum, M. Bouhassoune, J. Bouaziz, B. Schweflinghaus, S. Blügel, and S. Lounis, Nature communications 6, 8541 (2015).
- [46] M. Böttcher, S. Heinze, S. Egorov, J. Sinova, and B. Dupé, New Journal of Physics 20, 103014 (2018).
- [47] S. von Malottki, P. F. Bessarab, S. Haldar, A. Delin, and S. Heinze, Physical Review B 99, 060409 (2019).
- [48] A. Klautau, Physical Review B 105, 224413 (2022).
- [49] D. Capic, D. A. Garanin, and E. M. Chudnovsky, Journal of Physics: Condensed Matter 32, 415803 (2020).
- [50] L. Desplat, J.-V. Kim, and R. L. Stamps, Phys. Rev. B 99, 174409 (2019).
- [51] S. Sen, K. Somesh, R. Nath, and A. K. Nayak, Physical Review Applied 17, 044040 (2022).
- [52] S. Zhang, W. Wang, D. Burn, H. Peng, H. Berger, A. Bauer, C. Pfleiderer, G. Van Der Laan, and T. Hesjedal, Nature communications 9, 2115 (2018).
- [53] L. Peng, K. V. Iakoubovskii, K. Karube, Y. Taguchi, Y. Tokura, and X. Yu, Advanced Science 9, 2202950 (2022).
- [54] S. Huang, C. Zhou, G. Chen, H. Shen, A. K. Schmid, K. Liu, and Y. Wu, Physical Review B 96, 144412 (2017).
- [55] W. Koshibae and N. Nagaosa, Nature communications 5, 5148 (2014).
- [56] L. Kong and J. Zang, Phys. Rev. Lett. 111, 067203 (2013).
- [57] Y. Fei, Y. Fu, X. Bai, L. Du, Z. Li, H. Komber, K.-H. Low, S. Zhou, D. L. Phillips, X. Feng, et al., Journal of the American Chemical Society 143, 2353 (2021).
- [58] F. N. Rybakov and N. S. Kiselev, Phys. Rev. B 99, 064437 (2019).
- [59] A. Kirillov, E. Mintun, N. Ravi, H. Mao, C. Rolland, L. Gustafson, T. Xiao, S. Whitehead, A. C. Berg, W.-Y. Lo, et al., arXiv preprint arXiv:2304.02643 (2023).
- [60] B. Berg and M. Lüscher, Nucl. Phys. B 190, 412–424 (1981).
- [61] Q. Xu, O. Eriksson, and A. Delin, arXiv preprint arXiv:2309.17367 (2023).

A. Appendix

Figure 7 shows examples of scaling and perturbing DFT calculated parameters. The perturbing process perturbs parameters at each site with a resized Gaussian noise that samples from 0 to perturbation amplitude. In the scaling process, all parameters are called by the same scaling ratio.

The intuitive description of the blocking point is shown in 8 (a), it may have different shape in different cases

but the local topological charge distribution is always equal to zero. The real-space visualization and topological charge density figures for the array-like skyrmionic metamaterial build by prefabricated blocks with Q=-2, -5, and -12 are shown in (b)-(e), (c)-(f),(d)-(g), respectively.

Figure 9 denote real-space visualization and a schematic diagram of the blocking point and four kinds of site for the site-based topological charge distribution, respectively.

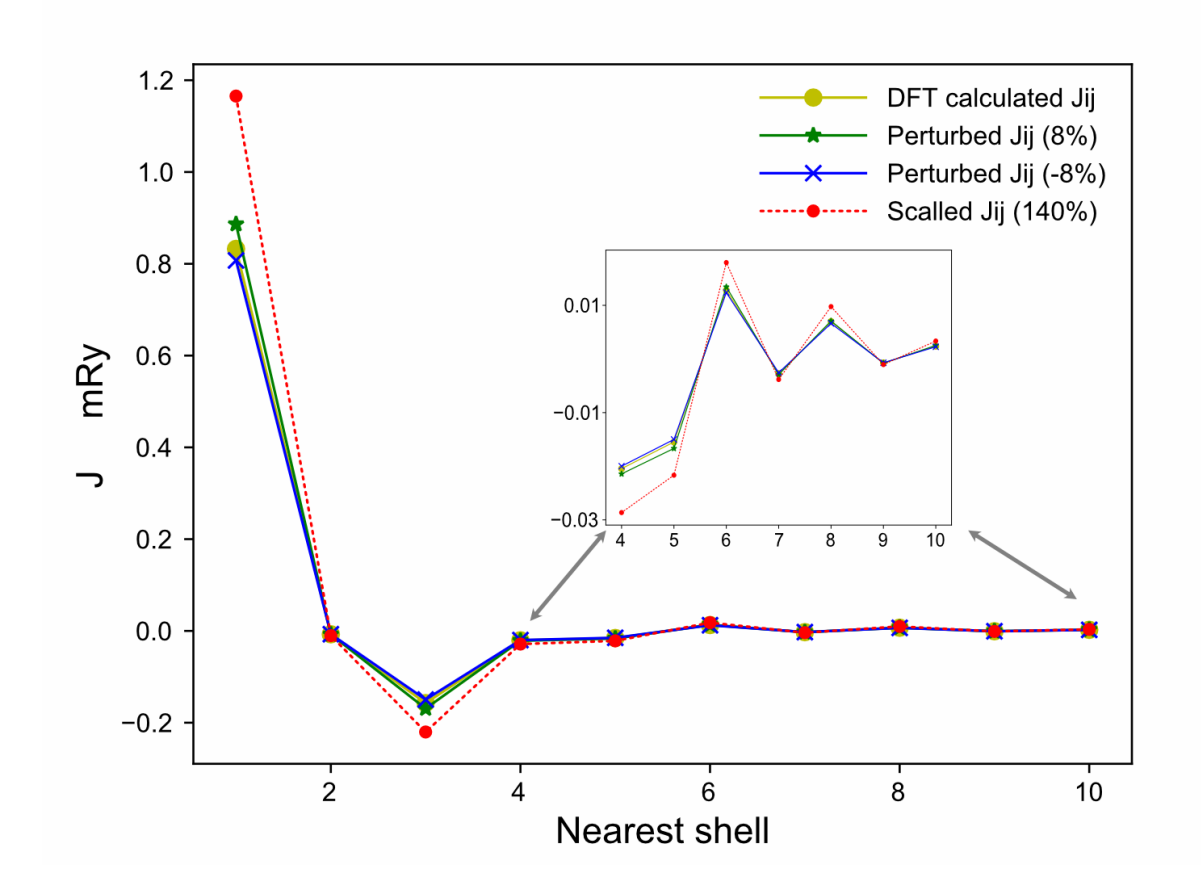


FIG. 7. Examples of scaling and perturbing DFT calculated parameters.

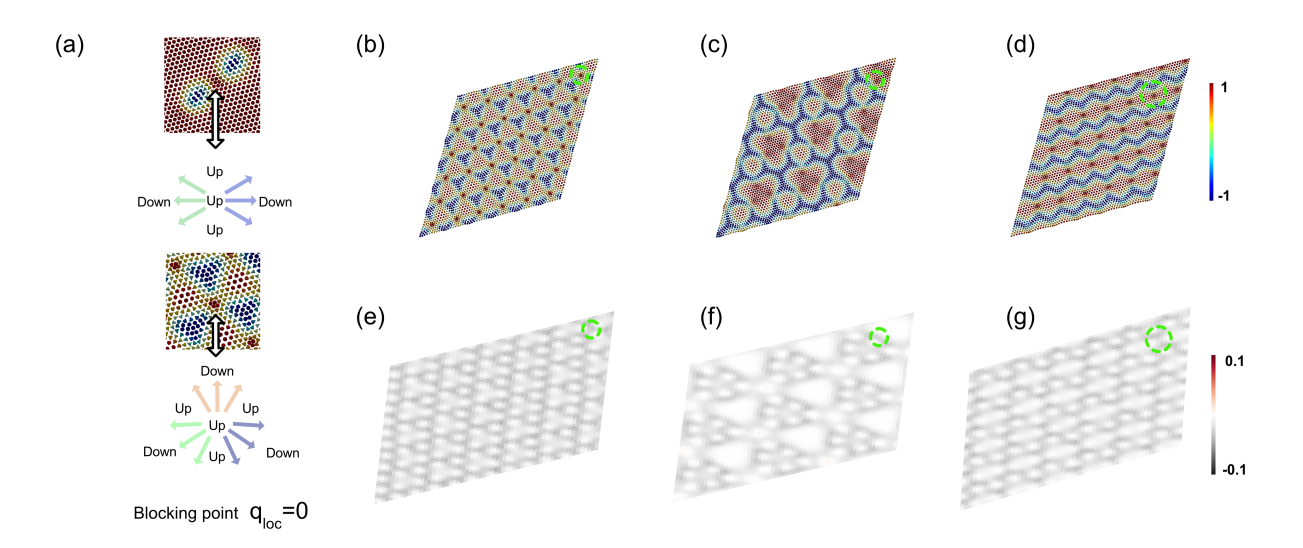


FIG. 8. (a) Real-space visualization and schematic diagram of blocking point between two antiskyrmions or Q=-2 high-order antiskyrmions. (b) Real-space visualization for an array-like skyrmionic metamaterial with Q=-2 high-order antiskyrmions (c) An array-like skyrmionic metamaterial formed from Q=-5 high-order antiskyrmions. (d) An array-like skyrmionic metamaterial composed of Q=-12 high-order antiskyrmions. (e-g) Topological charge density visualization for (b-d) The green dash cycle in (b-g) highlights one blocking point.

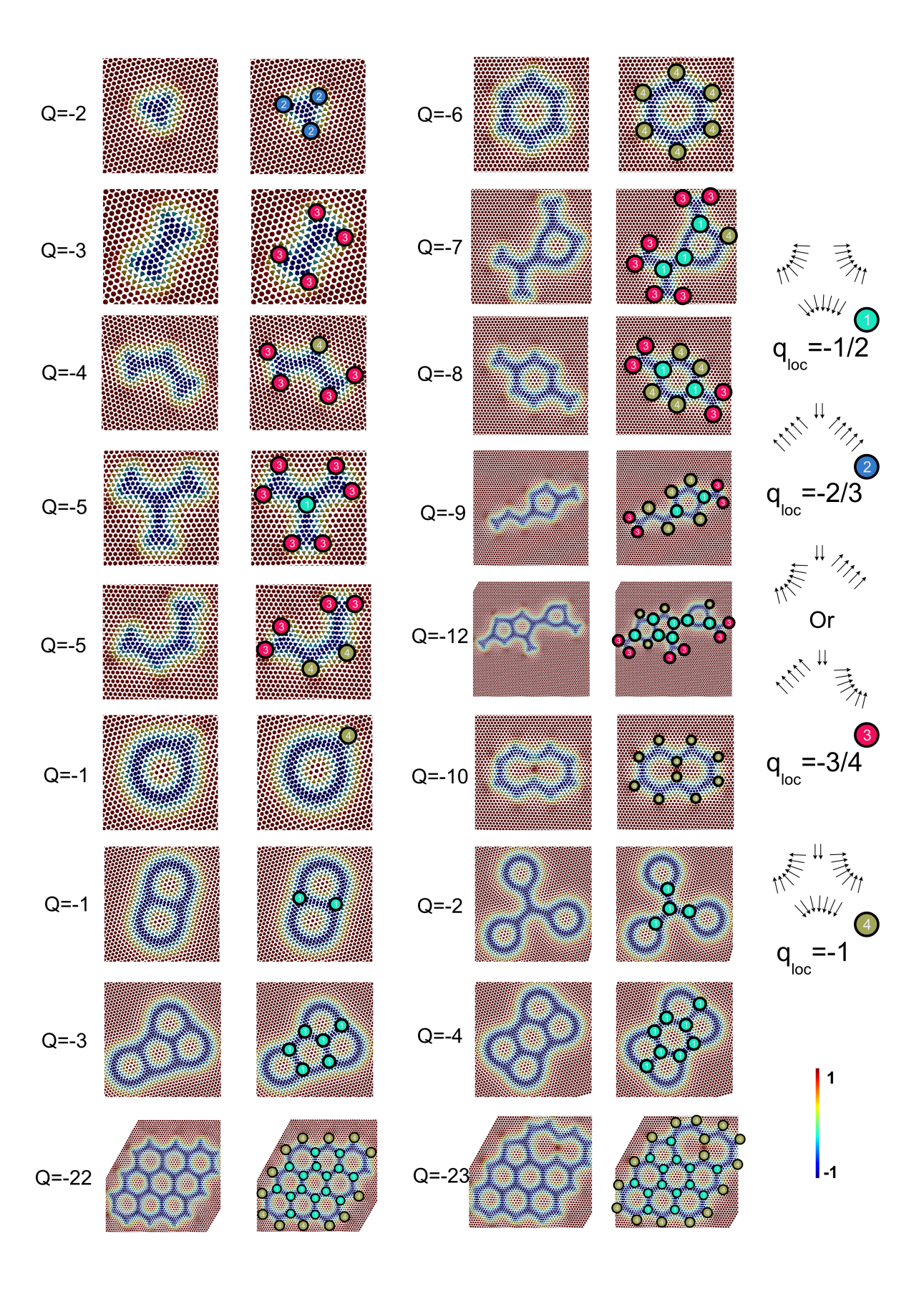


FIG. 9. Real-space visualization and schematic diagram of four kinds of site, which are used for the site-based topological charge distribution.